Axial Suspension Compliance and Compression for Enhancing Performance of a Nonlinear Vibration Energy Harvesting Beam System

R. L. Harne[1,2]
Department of Mechanical Engineering,
University of Michigan,
Ann Arbor, MI 48109-2125
e-mail: harne.3@osu.edu

K. W. Wang
Department of Mechanical Engineering,
University of Michigan,
Ann Arbor, MI 48109

Developing energy harvesting platforms that are strongly sensitive to the low and diffused frequency spectra of common environmental vibration sources is a research objective receiving great recent attention. It has been found that utilizing designs and incorporating structural influences that induce small values of linear stiffness may considerably enhance the power generation capabilities of energy harvesting systems. This research examines these two factors in new light toward the development of a biologically-inspired energy harvesting beam platform that exploits axial compressive effects and compliant suspensions. Through theory and experiments, it is found that the strategic exploitation of such characteristics promotes dramatic improvements in the average power that may be generated for the same excitation conditions. Examining the origin of these performance enhancements, it is seen that large compliance in the compressed axial suspensions facilitates a favorable redistribution of dynamic energy, which thereby enables greater bending of the harvester beam and increased electromechanical transduction. [DOI: 10.1115/1.4031412]

1 Introduction

The low and diffused frequency spectra of many common environmental vibration sources have recently focused research attention toward the development of energy harvesting device designs that are especially sensitive to such excitations. With the increased sensitivity come dynamic displacements of greater amplitude, which corresponds to increased power generation for many electromechanical transduction mechanisms. As such advancements are enabled, the conversion of the environmental vibrations into electrical power gradually becomes a more appealing and viable supply strategy for the ever-proliferating variety of low-power microelectronics in our world than the use of disposable batteries or direct line transmission [1]. While linear dynamics-based energy harvesting platforms may set theoretical performance limits [2], their numerous practical concerns—such as excessively large stroke motions at low frequencies and narrow bandwidths of operation—have encouraged researchers to explore performance enhancement approaches. These include multi degrees-of-freedom (DOF) structures [3,4], frequency conversion methodologies [5,6], and the deliberate incorporation of nonlinear designs and dynamics [7], each of which provides means to overcome the challenges of linear harvester platforms.

Among the numerous performance enhancement concepts, nonlinearities that induce small values of linear stiffness have been found to provide some of the most encompassing performance and operational benefits [2]. Green et al. [8] have shown that Duffing-type monostable nonlinearities favorably reduce the potential for damaging and large stroke motions as well as enhance the broadband response characteristics for energy harvesting from common, ambient vibration resources. Leadenham and Erturk [9] explored a device architecture that resulted in substantial bandwidth enhancement at low excitation levels by virtue of the large, nonlinear stretching capabilities in the M-shaped design. Meimukhin et al. [10] concluded that bistable Duffing nonlinearities are of particular benefit when bandlimited stochastic excitation levels are just sufficient to induce cross-well dynamic behaviors. This result agrees with the findings by Zhao and Erturk [11] regarding similar architectures under white noise excitation. Cao et al. [12] showed that variably inclined magnetic forces were a promising means to enhance the sensitivity of piezoelectric energy harvesters by means of a versatile restoring force tuning. The advancements are too many to adequately survey here; readers interested in greater details on the nonlinear energy harvesting developments that leverage small values of linear stiffness are referred to recent reviews [2,13].

The use of multiple dynamic elements in nonlinear energy harvesters has also been found to significantly enhance energy conversion capabilities. Tang and Yang [14] introduced a nonlinear piezoelectric harvester having an additional magnetic oscillator that led to enhanced peak power and broadened frequency sensitivity. Wu et al. [15] closely examined a 2DOF bistable energy harvesting architecture to exemplify that power *density* can also be magnified when integrating nonlinearity and multimodality. Recent findings by Chen and Jiang [16] analytically and numerically illustrated that 1:2 internal resonance in 2DOF energy harvesters may be a promising opportunity for enhanced performance under harmonic and stochastic excitations. Collectively, the results show that additional dynamic elements and an intelligent incorporation of nonlinearities leading to small linear stiffness values can provide a dramatic enhancement in the effectiveness of vibration energy harvesting systems.

These observations motivate this research to further investigate the strategic utilization of nonlinearities and additional elements to make traditional vibration energy harvesting platforms more sensitive to the low frequency and diffused spectra typical of ambient vibrations. Toward this end, a phenomenon found in

[1]Corresponding author.
[2]Present address: Department of Mechanical and Aerospace Engineering, The Ohio State University, Columbus, OH 43210.

Contributed by the Technical Committee on Vibration and Sound of ASME for publication in the JOURNAL OF VIBRATION AND ACOUSTICS. Manuscript received March 30, 2015; final manuscript received August 7, 2015; published online October 15, 2015. Assoc. Editor: Lei Zuo.

nature provides inspiration to this investigation, as discussed in the following paragraphs.

The wing motor mechanism in the fly (order Diptera) is recognized to be axially compressed such that the transverse motions connecting the motor to the wing are nonlinear and able to be magnified by modulation of the motor characteristics [17,18]. The mechanism is similar in construction and constraints to a simply supported beam that is axially compressed near to the elastic stability limit, which is the transition between mono- and bi-stability [19]. A schematic of the Dipteran wing motor is given in Fig. 1(*a*), as adapted and redrawn from Refs. [20,21]. The wing motor compression features are manipulated via supporting musculature, geometric factors, and inherent elasticities to induce large changes in the aerodynamic flapping force (flapping motions) without substantial variation in the level of input energy [18,21,22].

The flapping motion amplification that Diptera achieved by tailoring features of the wing motor suspension encourages this research to closely explore comparable architectural factors for vibration energy harvester enhancement. Building upon the wing motor inspiration, this investigation examines the influences of compressed axial suspension characteristics on the behaviors of an energy harvesting beam compressed near the elastic stability limit. The schematic model of the energy harvesting platform considered here is provided in Fig. 1(*b*), where the axial supporting elements (found at both ends of the central moving motor components in Diptera) are collected to one side of the simply supported piezoelectric beam. Rather than the conventional approach that directly compresses a beam simple support end to induce the nonlinearity, this investigation evaluates the strategic influences on the energy harvesting system performance effected by compressing the axial suspension spring which thereafter compresses the beam.

Section 2 introduces the experimental platform developed to examine the roles of axial suspension and compression on the energy harvesting system. Then, a model is derived to characterize the electromechanical dynamics in consequence to harmonic base acceleration. Numerical and analytical model solutions are realized and the theoretical predictions are compared to corresponding experimental measurements. The influences on the energy harvesting beam dynamics for changing axial suspension characteristics are explored in detail. Finally, a discussion is provided to elucidate the origin of the observed dynamical sensitivities that result from the variation in axial suspension and compression properties.

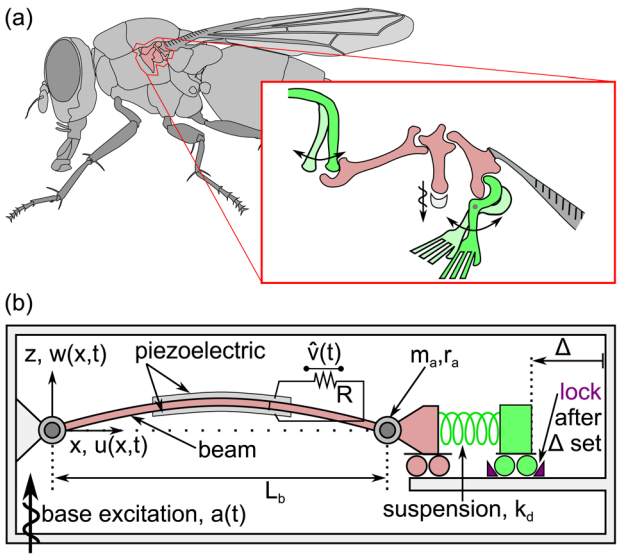

Fig. 1 (*a*) Schematic side view of a fly adapted and redrawn from Refs. [20,21], illustrating in the inset the wing motor mechanism and its flexibility via more lightly shaded elements and arrows indicating axial motion directions. (*b*) Biologically-inspired energy harvesting architecture explored in this study that incorporates dynamic axial suspension.

2 Experimental Platform Overview

A proof-of-concept experimental platform is fabricated in the laboratory to realize the energy harvesting system depicted in Fig. 1(*b*). The platform is shown in Fig. 2 and is centered around a simply supported spring steel beam. Several components are utilized to achieve the desired boundary conditions. The simply supported boundary conditions are realized by clamping small lengths of the spring steel beam ends into rotational guides which revolve on axles in low-friction bearings (McMaster-Carr, 8600N3). One of the simple supports is suspended axially using a pair of beams, which possess clamped–sliding boundary conditions; Fig. 2(*c*) illustrates the deformation characteristics of the suspension beams. Together, the suspension beams represent the equivalent one-dimensional axial spring that provides a net equivalent axial stiffness k_d. This stiffness is determined according to the assumptions of small deflection for each suspension beam which leads to the relation $k_s = 12E_sI_s/L_s^3$ [23] such that collectively $k_d = 2k_s$, and where $I_s = h_s t_s^3/12$. One end of each suspension beam is connected to the base of the system via a locked translational bearing, see Fig. 2(*b*). The opposite simple support boundary is able to glide on a free translation bearing and is compressed by distance Δ using a micrometer (Starrett 261). This compressive force acts on the simply supported beam as well as on the axial suspension spring. Once the compression distance Δ is set, the micrometer is locked using the built-in lock nut. Piezoelectric PVDF (Images Co., PZ-06) is bonded to both surfaces of the spring steel, simply supported beam near the center. By the arrangement and bonding, the piezoelectric layers are connected in series for maximum transduction, and the resulting electrical output generated by straining the beam and piezoelectric layers is fed to an external load resistance to evaluate the voltage and power generation performance of the system using the conventional assumption that a more complex electrical load is primarily resistive in effect. Finally, both of the boundary conditions of the beam—the suspension beam ends and the boundary which is compressed by the micrometer—are attached to an electrodynamic shaker (APS Dynamics 400) that provides for the base acceleration excitation considered here. The data acquired from experiments consists of the voltage $\hat{v}(t)$ across the external load resistance R, the displacement and velocity of the beam center point— $w(L/2,t)$ and $\dot{w}(L/2,t)$, respectively—via a laser interferometer (Polytec OFV 3001 S, OFV 303), and an accelerometer (PCB 352 C33) attached to the shaker.

A set of experiments are first conducted to provide motivating evidence that verifies the strategic importance of the axial suspension and compression characteristics in tailoring the overall dynamics of the energy harvesting system. To vary the equivalent stiffness of the axial suspension spring, the two supporting clamped–sliding beam lengths L_s are adjusted by the same amount, which influences the stiffness k_d according to the expression given in the previous paragraph. Figure 2(*c*) clarifies the strategy undertaken to change the length of a suspension beam to effect the desired deviation in equivalent suspension stiffness: the mounts to which they attach provide for multiple attachment points that may be selected among to vary the length L_s. Figure 3 presents the measured absolute value of the instantaneous voltage across a 5.0 MΩ load resistance when the system is excited with mean base acceleration of 3.43 m s^{-2} from 6 to 49 Hz, slowly sweeping at a rate of 0.112 Hz s^{-1}. The data sets are obtained with a constant applied axial force on the beams, such that the ratio of the applied compressive force $k_d\Delta$ is 4% greater than the Euler buckling load P_{cr} of the underlying simply supported beam. For each case of the suspension spring stiffness, the figure provides different shading hue to indicate the distinct data set; in addition, for such shading hue, a darker shading indicates the measurements obtained for an increasing sweep in the excitation frequency

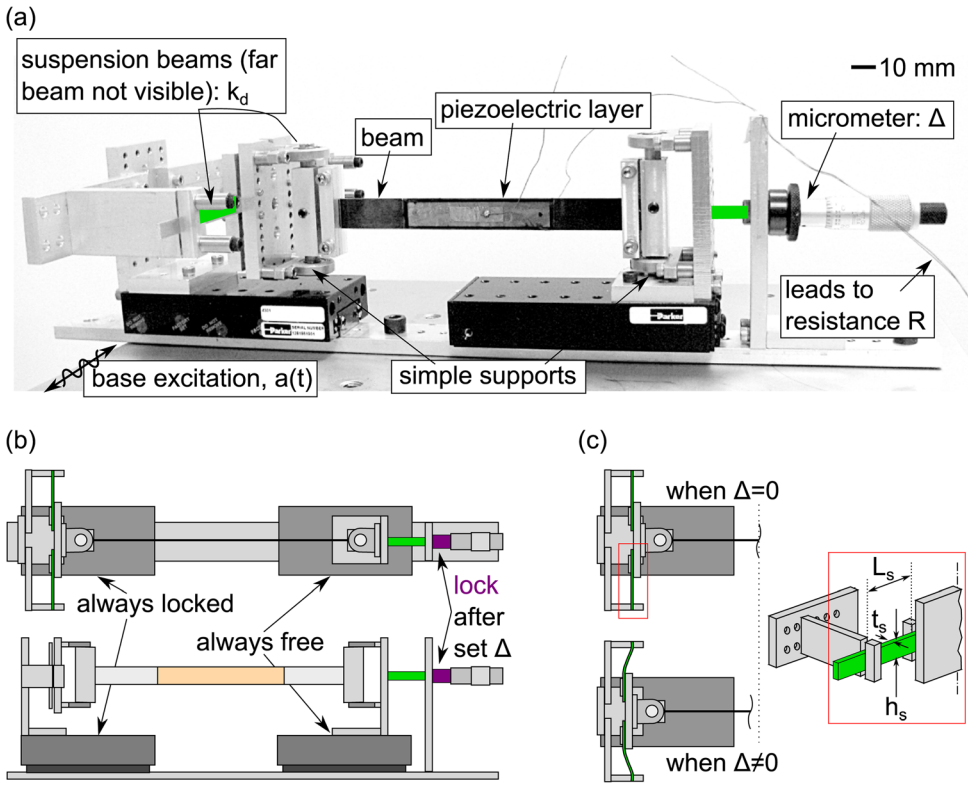

Fig. 2 Experimental, proof-of-concept energy harvester to examine the influence of axial suspension and compression characteristics. The equivalent axial suspension spring is realized by a pair of suspension beams whose lengths L_s are changed to govern the effective one-dimensional spring stiffness k_d. The system is compressed by distance Δ using the micrometer.

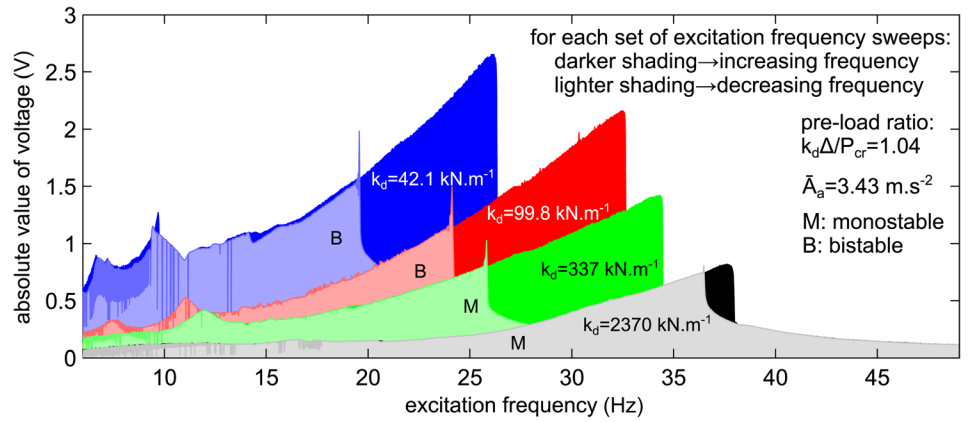

Fig. 3 Increasing and decreasing excitation frequency measurements for four cases of suspension spring stiffness using a mean base acceleration amplitude of 3.43 m s^{-2} and preload ratio of 1.04

whereas the respective lighter shading indicates the corresponding decreasing frequency sweep results. For a given suspension stiffness, these different sweep trajectories closely overlap for a substantial bandwidth of frequencies.

The trends in Fig. 3 give clear evidence that softer axial suspension stiffness leads to larger amplitudes in the transduced voltage across a wide range of excitation frequencies; as a result, the average power dissipated across the resistive load increases. Dynamic hysteresis is evident for each case of the suspension stiffness, shown by the differences in voltage amplitudes effected for upward and downward frequency sweeps. Such hysteresis is a common phenomenon for nonlinear dynamic systems and is here induced by the axial compressive force on the beam which is large enough such that it nearly or does in fact induce bistability, depending on the suspension stiffness k_d. For the cases $k_d = 337$ and 2370 kN m^{-1}, the energy harvesters are monostable (label M in Fig. 3) due to the applied compressive axial force, whereas the cases of $k_d = 42.1$ and 99.8 kN m^{-1} are statically and dynamically bistable (label B). The data show that the amplification of the voltage for softer axial suspension stiffnesses is particularly evident at lower frequencies of excitation, which is favorable in light of the typical low frequency spectra of common ambient vibrations. All together, the measurements presented in Fig. 3 suggest that a substantial sensitivity is able to be leveraged in the axially suspended

energy harvesting system for voltage (and hence power) generation enhancement, which motivates the remainder of this research.

Finally, although the average powers obtained by the platforms evaluated in Fig. 3 are only on the order of a few hundred nanowatts, it is recognized that load impedance matching to the piezoelectric PVDF layers and/or the utilization of more strongly coupled piezoelectric materials may improve these power quantities. Yet, rather than focus on such features that lead to optimal designs, this study examines the roles that the axial suspension and compression characteristics play toward enhancing the overall power generation capabilities of the energy harvesting beam system. These roles are reflective of the performance potential specifically enabled by such characteristics whether they are exploited on the current proof-of-concept platform or when using a harvester device having impedance matched load and/or strongly coupled piezoceramic layers.

3 Model Framework and Solution Methods

3.1 Governing Equations of Motion. To develop such a theoretical understanding of the sensitivities induced in consequence to the dynamic axial suspension features, the equations of motion of the energy harvesting system are derived using energy principles [24]. The simply supported beam undergoes transverse/bending and axial deflections $w(x,t)$ and $u(x,t)$, respectively. The bending curvature of the beam is expressed by $\psi = w_{xx}(1-w_x^2)^{-1/2}$, where subscript x indicates a spatial partial derivative and the curvature expression takes into account large deflections [25]. According to experimental observations, the modeling neglects the effects of transverse shearing, beam and piezoelectric rotary inertia, and beam and piezoelectric axial inertia. Due to the practical implementation of simply supported beam boundary conditions, point masses having moments of inertia $m_a r_a^2$ are considered to be located at the beam ends. The piezoelectric layers are assumed to be perfectly bonded to the beam. As shown in Fig. 1(*b*), the energy harvesting beam is excited by harmonic motions of its surrounding frame $\ddot{a}(t) = A_a \cos \Omega t$, where A_a is the acceleration amplitude and $\Omega/2\pi$ is the excitation frequency in Hz. A body force $s(x)$ acts along the length of the beam, which may represent gravitational effects depending on the harvester configuration; body force influences on the piezoelectric layers are presumed to be comparatively insubstantial. Taking into account the above assumptions, the Lagrangian of the system is expressed, $L = T + W_e - U$, where T are the kinetic, W_e are the electrical and electromechanical, and U are the potential energies [26].

$$T = \frac{1}{2}\rho_b A_b \int_0^{L_b} (\dot{w}+\dot{a})^2 \mathrm{d}x + \frac{1}{2} 2\rho_p A_p \int_{l_1}^{l_2} (\dot{w}+\dot{a})^2 \mathrm{d}x + \frac{1}{2}\left(\frac{1}{2} m_a r_a^2\right)\left(\frac{\partial \dot{w}}{\partial x}\bigg|_{x=0}\right)^2 + \frac{1}{2}\left(\frac{1}{2} m_a r_a^2\right)\left(\frac{\partial \dot{w}}{\partial x}\bigg|_{x=L_b}\right)^2 \tag{1}$$

$$W_e - U = \frac{1}{2} 2\left(\frac{A_p}{t_p^2}\right)\int_{l_1}^{l_2} \varepsilon_{33}\dot{\hat{\lambda}}^2 + 2\left(\frac{A_p \bar{t}_p}{t_p}\right) e_{31} \times \int_{l_1}^{l_2}\left[w_{xx} + \frac{1}{2} w_{xx} w_x^2\right]\dot{\hat{\lambda}}\mathrm{d}x - \frac{1}{2} E_b A_b \int_0^{L_b}\left[u_x + \frac{1}{2} w_x^2\right]^2 \mathrm{d}x - \frac{1}{2} E_b I_b \int_0^{L_b}\left[w_{xx}^2 + w_{xx}^2 w_x^2\right]\mathrm{d}x - \frac{1}{2} 2E_p I_p \int_{l_1}^{l_2}\left[w_{xx}^2 + w_{xx}^2 w_x^2\right]\mathrm{d}x - \frac{1}{2} k_d u^2\Big|_{x=L_b} - k_d \Delta \int_0^{L_b} u_x \mathrm{d}x - \int_0^{L_b} s(x) w \mathrm{d}x \tag{2}$$

The operators $(\cdot)$ and $()_x$ indicate differentiation with respect to time t and beam length coordinate x, respectively. Other parameters are as follows, where subscript b indicates the term is related to the beam while subscript p indicates the term refers of the piezoelectric layers: volumetric densities $\rho_{b,p}$; areas $A_{b,p}$; widths $h_{b,p}$; thicknesses $t_{b,p}$; beam natural length L_b; beginning and ending piezoelectric PVDF material positions along the beam length $l_{1,2}$; centroid of the piezoelectric layers from the beam midplane $\bar{t}_p$; piezoelectric material permittivity at constant strain ε_{33}; piezoelectric bending constant e_{31}; flux linkage $\hat{\lambda}$ such that $\dot{\hat{\lambda}} = \hat{v}$ is the voltage across the electrodes; radius r_a of the rotational mass m_a; Young's moduli $E_{b,p}$; and moments of inertia $I_{b,p}$.

A dissipation function, D, is introduced to include the effects of the primary mechanical and electrical damping phenomena

$$D = \frac{1}{2} c_b \int_0^{L_b} \dot{w}^2 \mathrm{d}x + \frac{1}{2}\left(\frac{1}{R}\right)\dot{\hat{\lambda}}^2 \tag{3}$$

where c_b is the viscous damping per beam length.

The transverse and axial beam motions are expanded as a summation of trial functions [27]

$$u(x,t) = \sum_{n=1}^{\infty} \hat{f}_n(t)\alpha_n(x) = \sum_{n=1}^{\infty}\left[\hat{f}_n(t)\left(c_{n,1}x + c_{n,2}\sin\frac{2n\pi x}{L_b}\right)\right] \tag{4}$$

$$w(x,t) = \sum_{n=1}^{\infty} \hat{g}_n(t)\phi_n(x) = \sum_{n=1}^{\infty} \hat{g}_n(t)\sin\frac{n\pi x}{L_b} \tag{5}$$

According to the frequencies of excitation considered here as well as the shape of the beam deflections induced in the experimentation, it is safely assumed that only the fundamental mode responses contribute to the overall displacement dynamics in the energy harvesting beam

$$u(x,t) = \hat{f}_1 x + \hat{f}_2 \sin\frac{2\pi x}{L_b} \tag{6}$$

$$w(x,t) = \hat{g}\sin\frac{\pi x}{L_b} \tag{7}$$

The generalized coordinates of the system are thus $\mathbf{q} = [\hat{f}_1, \hat{f}_2, \hat{g}, \hat{\lambda}]^{\mathrm{T}}$. In other words, the four coordinates include the two for axial motions of the beam $(\hat{f}_1, \hat{f}_2)$, one for beam bending $(\hat{g})$, and a final coordinate for the flux linkage $(\hat{\lambda})$ across the load resistance R. Applying Lagrange's equations,

$$\frac{\partial}{\partial t}\left[\frac{\partial L}{\partial \dot{q}_i}\right] + \frac{\partial D}{\partial \dot{q}_i} - \frac{\partial L}{\partial q_i} = 0 \tag{8}$$

leads to the governing equations for the generalized mechanical and electrical coordinates of the energy harvesting system. By this approach, it is found that the coordinates $\hat{f}_1$ and $\hat{f}_2$ are able to be expressed directly in terms of the bending generalized coordinate $\hat{g}$.

$$\hat{f}_1 = -\left(\frac{k_d \Delta}{E_b A_b}\right)\frac{1}{\kappa+1} - \frac{1}{4}\left(\frac{\pi}{L_b}\right)^2 \frac{1}{\kappa+1}\hat{g}^2 \tag{9}$$

$$\hat{f}_2 = -\frac{1}{8}\left(\frac{\pi}{L_b}\right)\hat{g}^2 \tag{10}$$

where the axial stiffness ratio is defined as the ratio between the axial suspension spring stiffness k_d and the beam axial stiffness

$$\kappa = \frac{k_d L_b}{E_b A_b}$$

Then, continued use of Lagrange's equations leads to

$$C_p^*\ddot{\hat{\lambda}} + \frac{1}{R}\dot{\hat{\lambda}} = -\theta^*\dot{\hat{g}} - \theta_{\mathrm{NL}}^*\dot{\hat{g}}^3 \tag{12}$$

where the coefficients with superscript * are specified in the Appendix. The capacitance of the piezoelectric layers is C_p^*, while the linear and nonlinear electromechanical coupling terms are θ^* and θ_{NL}^*, respectively. Using the relationship that the time rate of change of flux linkage is the voltage across the load: $\dot{\hat{\lambda}} = \hat{v}$, Eq. (12) is rewritten to be

$$C_p^*\dot{\hat{v}} + \frac{1}{R}\hat{v} = -\theta^*\dot{\hat{g}} - \theta_{\mathrm{NL}}^*\dot{\hat{g}}^3 \tag{13}$$

Then, Lagrange's equations are applied to the bending generalized coordinate $\hat{g}$. Following the adoption of nondimensional beam displacement $g = \hat{g}/L_b$, voltage $v = \hat{v}(C_p^*/\theta^* L_b)$ and time $\tau = \omega_0 t$, where ω_0 is the uncompressed beam fundamental natural frequency, the nonlinear electromechanical terms are then neglected, and finally a series of simplifications leads to the coupled, nonlinear governing Eqs. (14) and (15) for the energy harvesting system

$$\begin{aligned} g'' + \eta g' + \left[1 - \frac{k_d\Delta}{P_{cr}}\frac{1}{\kappa+1}\right]g + \left[\beta + \gamma\frac{\kappa}{\kappa+1}\right]g^3 \\ = -h + \theta v + z\cos\omega\tau \end{aligned} \tag{14}$$

$$v' + \alpha v = -g' \tag{15}$$

where the operator $()'$ indicates differentiation with respect to nondimensional time τ. The following coefficients are defined:

$$\omega = \frac{\Omega}{\omega_0};\quad \omega_0^2 = \frac{K^*}{M^*};\quad P_{\mathrm{cr}} = \frac{K^*}{K_p^*};\quad \eta = \frac{C^*}{M^*\omega_0};\quad \beta = \frac{F_1^* L_b^2}{K^*} \tag{16}$$

$$\gamma = \frac{F_2^* L_b^2}{K^*};\quad h = \frac{H^*}{K^* L_b};\quad z = -\frac{Z^* A_a}{K^* L_b};\quad \alpha = \frac{1}{RC_p^*\omega_0};\quad \theta = \frac{(\theta^*)^2}{C_p^* K^*} \tag{17}$$

In Eqs. (14) and (15), the term $k_d\Delta/P_{\mathrm{cr}}$ is the axial preload ratio, defined as the ratio of axial compressive force (realized by displacing the axial suspension spring a distance Δ) to the fundamental Euler buckling force P_{cr}.

3.2 Approximate Analytical Solution to the Governing Equations. The oscillations of the mechanical and electrical displacements are assumed to primarily be proportional to the same frequency as the base acceleration excitation. This assumption is strongly borne out in the experimentation conducted here, according to the system design parameters considered. As a result, the periodic motions of the system are approximated by fundamental Fourier series expansions for each nondimensional generalized coordinate in Eqs. (14) and (15).

$$g(\tau) = c(\tau) + a(\tau)\sin\omega\tau + b(\tau)\cos\omega\tau \tag{19}$$

$$v(\tau) = m(\tau)\sin\omega\tau + n(\tau)\cos\omega\tau \tag{20}$$

The coefficient $c(\tau)$ is necessary in the event that the energy harvesting beam is compressed to a degree that induces bistability, in which case a nonzero mean displacement of oscillation may be obtained for certain excitations. The time dependence of the coefficients is necessary in order to predict the stability of the periodic orbits obtained via this approximate analytical solution method. Additional terms are defined

$$r^2(\tau) = a^2(\tau) + b^2(\tau) \tag{21}$$

$$A = 1 - \frac{k_d\Delta}{P_{\mathrm{cr}}}\frac{1}{\kappa+1} \tag{22}$$

$$B = \beta + \gamma\frac{\kappa}{\kappa+1} \tag{23}$$

Then, the assumed solution forms in Eqs. (19) and (20) are substituted into Eqs. (14) and (15). Higher-order harmonics are neglected, the coefficients are assumed to vary slowly but finite in time, and the resulting harmonic coefficient terms are collected to yield the following modulation equations:

$$-\eta c' = \left[A + B\left(c^2 + \frac{3}{2}r^2\right)\right]c + h \tag{24}$$

$$-\eta a' + 2\omega b' = \left[A - \omega^2 + B\left(3c^2 + \frac{3}{4}r^2\right)\right]a - \eta\omega b - \theta m \tag{25}$$

$$-2\omega a' - \eta b' - z = \eta\omega a + \left[A - \omega^2 + B\left(3c^2 + \frac{3}{4}r^2\right)\right]b - \theta n \tag{26}$$

$$-a' - m' = -\omega b + \alpha m - \omega n \tag{27}$$

$$-b' - n' = \omega a + \omega m + \alpha n \tag{28}$$

which may be compactly expressed by defining $\mathbf{x} = [c, a, b, m, n]^{\mathrm{T}}$ such that

$$\mathrm{P}\mathbf{x}' = \mathrm{G}\mathbf{x} + h[1, 0, 0, 0, 0]^{\mathrm{T}} \tag{29}$$

where the matrices P and G are determined accordingly. The algebraic modulation Eqs. (24)–(28) are then sequentially solved, with the results successively substituted into each other. By summing and squaring the two final equations which cannot otherwise be reduced further, this process yields a sixth-order response polynomial in terms of the energy harvester displacement amplitude r (or third-order in terms of r^2 when $h = 0$). Finally, all of the coefficients in $\mathbf{x}$ may be solved for in terms of the displacement amplitude r to reconstruct the analytically predicted solution for time dependence upon the bending and voltage generalized coordinates via Eqs. (19) and (20).

The roots of the polynomial in r are mathematical solutions but not necessarily physically meaningful since they may not be dynamics that are able to be observed in experimentation. Thus, the stability of each resulting solution set $\mathbf{x}^*$ stemming from a root r is evaluated. In this work, stability is determined by linearizing the system response around the solution and classifying the eigenvalue components of the resulting Jacobian matrix $\mathrm{J} = [\mathrm{d}(\mathrm{P}^{-1}\mathrm{G})/\mathrm{d}\mathbf{x}]|_{\mathbf{x}=\mathbf{x}^*}$. Stable predicted solutions yield eigenvalues having negative real components [28].

For a given set of system and excitation parameters, the stable solutions (the coefficients $\mathbf{x}^*$) are then used to calculate the beam deflections $w(x,t)$ and $u(x,t)$ and the transduced voltage $\hat{v}(t)$ across the load resistance R. Consequently, the average power is quantified by $P = |\hat{v}|^2/2R$.

3.3 Numerical Solution of the Governing Equations. To supplement the approximate analytical solutions, the governing Eqs. (14) and (15) are solved by numerical integration based on a fourth-order Runge–Kutta algorithm using MATLAB. The numerical integrations are conducted for 2000 periods of excitation for any given excitation frequency considered; this time span is chosen to ensure that steady-state behaviors are fully developed. For a given set of system and excitation parameters, the numerical evaluations are conducted 20 times using randomly selected initial conditions

(displacement, velocity, and voltage) for each run, so as to sample a broad range of the initial condition space and uncover all possible steady-state oscillation forms. Finally, with such data sets, the fast Fourier transforms of the displacement, velocity, and voltage are taken over the last 50% of the time series; then, the spectral amplitudes proportional to the excitation frequency Ω are kept since these are the corresponding dynamic features which are represented via the analytical Fourier series approximations in Eqs. (19) and (20). This is likewise the data processing method employed in experimentation to extract the measured dynamic contributions proportional to the excitation frequency.

4 Roles of Axial Suspension Stiffness and Compression Characteristics on Voltage Generation

Through a series of analytical, numerical, and experimental studies, this section examines the roles played by the axial suspension properties and compression features toward tailoring the dynamical behaviors which lead to favorable voltage transduction from the energy harvesting platform. The parameters used in the model for numerical and analytical results are given in Table 1 and are identified experimentally with the exception of permittivity ε_{33} and the piezoelectric material thickness t_p, which are taken from the manufacturer specifications. The loss factor η is dynamically identified from experiments of driven, steady-state vibration [29] while the beam is uncompressed. Due to the alignment of the platform during experimentation, there are no body forces to account for, which prescribes $s(x) = 0$ in the model. According to the suspension stiffnesses as given in Table 1, the corresponding axial stiffness ratios are $\kappa \equiv k_d L_b / E_b A_b = [0.0053, 0.0126, 0.0426, 0.300]$.

To compare the energy harvesting beams with *compliant* axial simple supports under study and a beam having *fixed* axial supports, one of the platforms is experimentally evaluated with the suspending beams/springs removed such that the simple support of this beam end is fixed to the locked translational bearing, so as to prevent axial motions. Since the opposing end of this harvester beam is axially compressed using the micrometer, ideally this case should effect an axial stiffness ratio of $\kappa = \infty$ so that one could refer to this harvester design as the "conventional" simply supported and axially compressed platform. However, it is found that there exists considerable deviation in the measurements acquired using this axially "fixed–fixed" design with the analytical predictions obtained using $\kappa = \infty$. Upon inspection, the discrepancy is identified to be the fact that the experimentally vibrating beam may axially stretch *away* from the micrometer tip since this beam end is not constrained to maintain axial contact with the micrometer tip so as to satisfy the ideal boundary condition of the related axial force $k_d\Delta$. Through iterative comparisons, it is found that the measurements using the axially fixed–fixed harvester beam are in greater agreement to analytical predictions using an axial stiffness ratio $\kappa = 0.300$. Therefore, although this experimental design does not realize the ideal axially fixed–fixed boundary conditions, hereafter the case of $\kappa = 0.300$ will be referred to as the conventional case since it represents the set of boundary conditions that most closely approximate the beam supports that have no compliant suspensions.

All designs employing axial suspensions may suffer from the possibility that the beams may dynamically stretch away from the micrometer tip. This is because it is difficult to enforce the ideal boundary condition of an applied axial force $k_d\Delta$ that accommodates axial motions satisfying assumptions of the Euler–Bernoulli beam theory. But the concern is most relevant for the axially fixed–fixed design where all of the system axial compliance is concentrated in the beam elasticity itself. Once additional axial compliance is introduced by the axial suspension, the concern of the beam translating away from the micrometer tip is drastically reduced, as is evident in the experiments. Thus, unlike the conventional axially fixed–fixed case, it is found that there is no need to compensate the parameter identification for the cases $\kappa = [0.0053, 0.0126, 0.0426]$, which are computed exactly from the definition of κ with respect to the system designs.

For frequency sweep experiments, the base acceleration amplitude A_a is found to slightly vary over the course of exciting the structure from 6 to 49 Hz, and then returning to 6 Hz. As a result, the exact measured base acceleration amplitudes are used as input to the analytical and numerical modeling, and the mean value of the amplitude $\bar{A}_a$ is reported here. As a final note before the following studies, because of the relations among the linear stiffness term in Eq. (14), a preload ratio $k_d\Delta/P_{cr}$ value greater than unity may not necessarily induce bistability, as is the case for the ideal simply supported beam. Consequently, to differentiate the dynamical behaviors according to the static structural properties, the plots of analytical and experimental results presented below denote that the underlying energy harvesting beam is monostable when the curves are dotted, whereas the solid curves indicate the beam is compressed to a degree that induces bistability.

Table 1 Identified experimental system parameters

L_b (mm)	$h_{b,p}$ (mm)	t_b (mm)	E_b (GPa)	ρ_b (kg m^{-3})
147	12.7	0.508	180	8000
$l_{1,2}$ (mm)	t_p (mm)	E_p (GPa)	ρ_p (kg m^{-3})	$k_{d(1-4)}$ (kN m^{-1})
54.4, 92.5	0.0286	1.80	1800	42.1, 99.8, 337, 2370
ε_{33} (F m^{-1})	e_{31} (C m^{-2})	R (MΩ)	$m_a r_a^2$ (kg m^2)	η
110×10^{-12}	0.017	5.0	8.125×10^{-7}	0.0367

4.1 Voltage Transduction Achieved Using Moderate Axial Compressive Force. When the preload ratio $k_d\Delta/P_{cr}$ is 0.70, all of the harvester designs examined here are monostable. Figure 4(*a*) plots the experimentally measured amplitudes of voltage

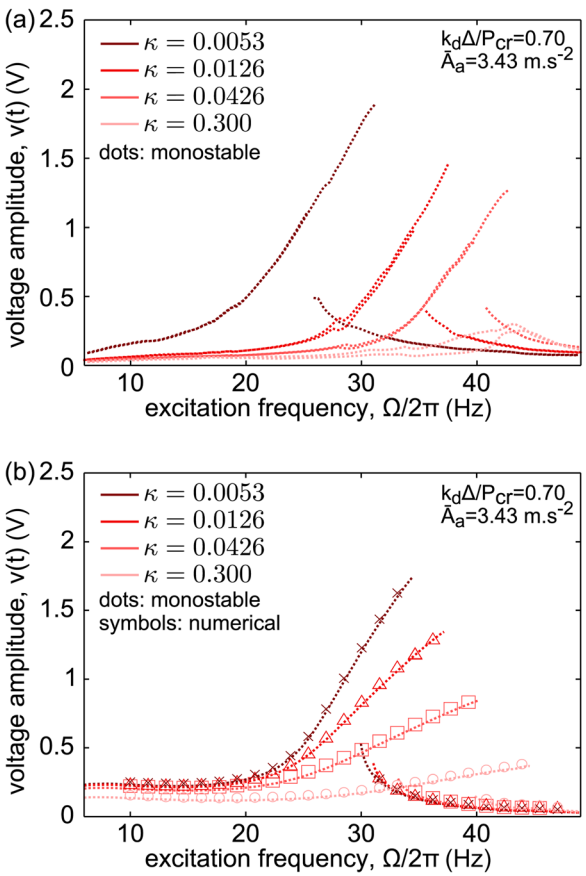

Fig. 4 Voltage across load resistance for preload ratio of 0.70 and mean base acceleration level 3.43 m s^{-2}: (*a*) experimental measurements and (*b*) analytical and numerical results

across the load resistance, corresponding to the spectral component proportional to the excitation frequency. Figure 4(*b*) presents the corresponding analytical and numerical results using curves and symbols, respectively, when the mean amplitude of base acceleration is 3.43 m s^{-2} and the frequency is slowly swept up/down at a rate of 0.112 Hz s^{-1} in the range of 6–49 Hz. The increasing shading darkness of curves or data points represents decreasing axial spring stiffness, characterized via the axial stiffness ratio κ. The results indicate that the platforms having progressively decreasing axial suspension stiffness lead to gradually enhanced levels of peak voltage amplitude. The analytical and numerical results are in good agreement to such trends with respect to the measurements. The effect of the softer suspension stiffnesses is an enhanced sensitivity of the devices to the lower frequency excitations, thus providing considerable amplification of the voltage when compared to the stiffer suspension designs. For example, according to the measurements, using the most compliant design having $\kappa = 0.0053$ leads to 20 times greater voltage amplitude than the conventional simply supported platform of $\kappa = 0.300$ at an excitation frequency of 25 Hz. In other words, the strategic exploitation of the compliant axial boundary enhances the average power generation by 400 times while the excitation conditions remain the same. Such a result has clear analogy to the manipulation by Diptera of wing motor suspension characteristics so as to obtain greater amplitudes of flapping force without substantial deviation in the input energy level.

4.2 Influences of Suspension Stiffness and Increased Axial Compressive Force. The qualitative behaviors and performance of the energy harvesters change significantly when the axial compressive force is increased. Figure 5 shows the results of increasing the preload ratio to 1.04 for all of the designs considered here. Based upon the axial stiffness ratios, only the cases of $\kappa = 0.0053$ and 0.0126 (respectively, $k_d = 42.1$ and 99.8 kN m^{-1}) are statically bistable, evident via the solid curve line styles in Fig. 5. For such an axial compressive force, the platform using $\kappa = 0.0426$ is only marginally monostable, since the preload ratios to induce bistability are $k_d\Delta/P_{cr} > 1.0426$.

Although the same overall influence is observed in Fig. 5 regarding the enhancement of voltage output that results from the decrease in axial suspension stiffness as was evident in Fig. 4, the magnification of voltage amplitude is seen to be more pronounced at low frequencies in Fig. 5 due to the greater preload ratio of 1.04. This characteristic is particularly apparent via the analytical and numerical results in Fig. 5(*b*). Experimentally, it is found that additional friction forces due to the simple support bearings—not accounted for in the model—increase damping phenomena at low excitation frequencies, which has the effect of potentially inhibiting the large amplitude harvester dynamics. That factor aside, the measurements still show that > 70 times enhancement in average power may be leveraged at 14.5 Hz by replacing a conventional axial simple support design ($\kappa = 0.300$) with the most axially compliant design examined here ($\kappa = 0.0053$).

When the frequency of excitation is fixed at 16 Hz, the influence of change in base acceleration amplitude is uncovered in Fig. 6. Experimentally, the amplitude of the base acceleration is slowly varied at a rate of 0.092 m s^{-3} from 0 m s^{-2} to 6 m s^{-2}. This excitation frequency is one at which an apparent discrepancy appears between the voltage amplitudes measured experimentally with respect to those determined by the model (see Fig. 5), due to the friction forces in the simple support bearings. Nevertheless, both the measurements of Fig. 6(*a*) and model predictions in Fig. 6(*b*) agree that the voltage enhancement resulting from reduced axial suspension stiffness is a benefit that can be leveraged across a broad range of base acceleration amplitudes. At the same time, the results of Figs. 4–6 collectively reveal an additional influence of importance. Whether for preload ratio of 0.70 or 1.04, the figures show that an increased likelihood of triggering coexisting dynamics is also a consequence of the softer

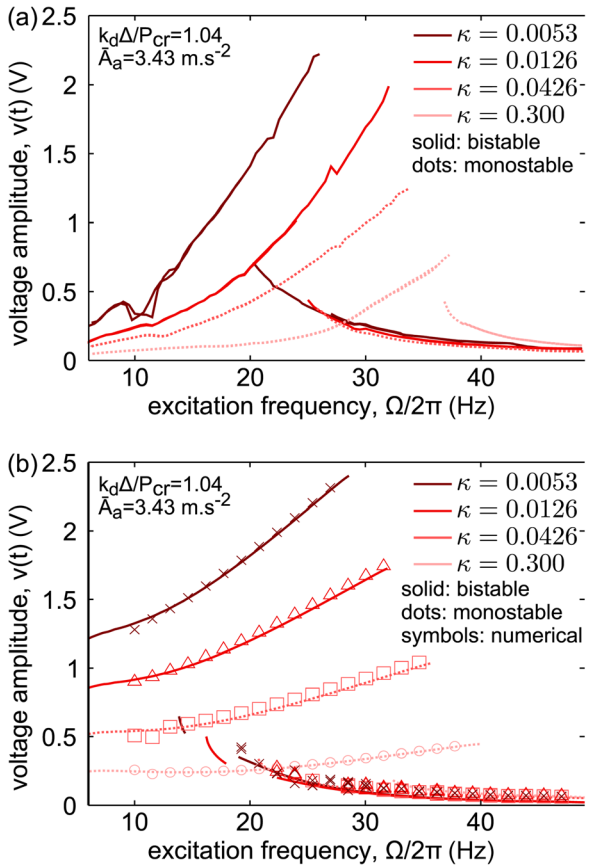

Fig. 5 Voltage across load resistance for preload ratio of 1.04 and mean base acceleration level 3.43 m s^{-2}: (*a*) experimental measurements and (*b*) analytical and numerical results

suspensions. In other words, due to the degree of axial compressive forces, the energy harvesters exhibit considerable nonlinearity in the dynamical behaviors, which becomes manifest as an initial condition-dependent steady-state oscillation. Coexisting dynamics, which have the parallel consequence of inducing coexisting voltage magnitudes and powers, are a particular drawback to the exploitation of nonlinearity in energy harvesting platforms [2,13]: one dynamic tends to be of substantially greater benefit than the other. As a result, the valuable utilization of these nonlinearities requires careful attention to system design and implementation so that the potential for adverse coexisting dynamics is minimized according to anticipated operating conditions.

Figure 7(*a*) presents phase portraits in the plane of voltage across the load resistance and the energy harvesting beam center point bending displacement, using the measurements taken at 16 Hz and base acceleration amplitude of 2.17 m s^{-2}. As shown in Fig. 6(*a*), two coexisting dynamics occur for the platform when the axial stiffness ratio is 0.0053. Since the harvester platform is bistable under this preload ratio of 1.04, either an intrawell or snap-through steady-state dynamic is possible, based upon the initial conditions of displacement and velocity. The intrawell dynamics are those which oscillate around a stable equilibrium of displacement, whereas the snap-through motions are energetic behaviors that cross the unstable, near-central equilibrium twice per cycle of oscillation [30]. The results of Fig. 7(*a*) reveal that more than an 18 times difference in average power exists between the regimes, where the favorable steady-state dynamic for energy harvesting is the snap-through regime. Although methods have been explored to "escape" the undesirable intrawell oscillation [31], the proposed interventions have so far required energy input to perturb the energy harvester from an otherwise stable, dynamic steady-state. Thus, intelligent implementation of such nonlinear

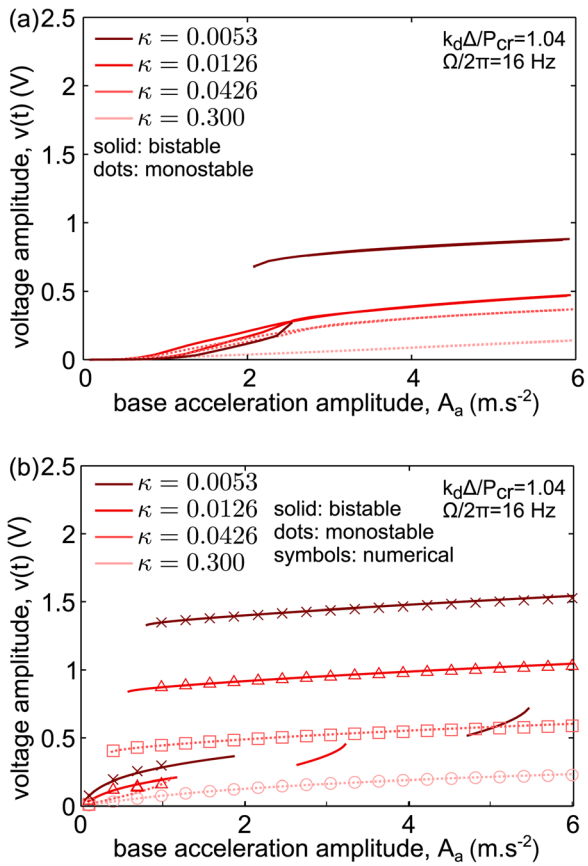

Fig. 6 Voltage across load resistance for preload ratio of 1.04 and excitation frequency of 16 Hz: (*a*) experimental measurements and (*b*) analytical and numerical results

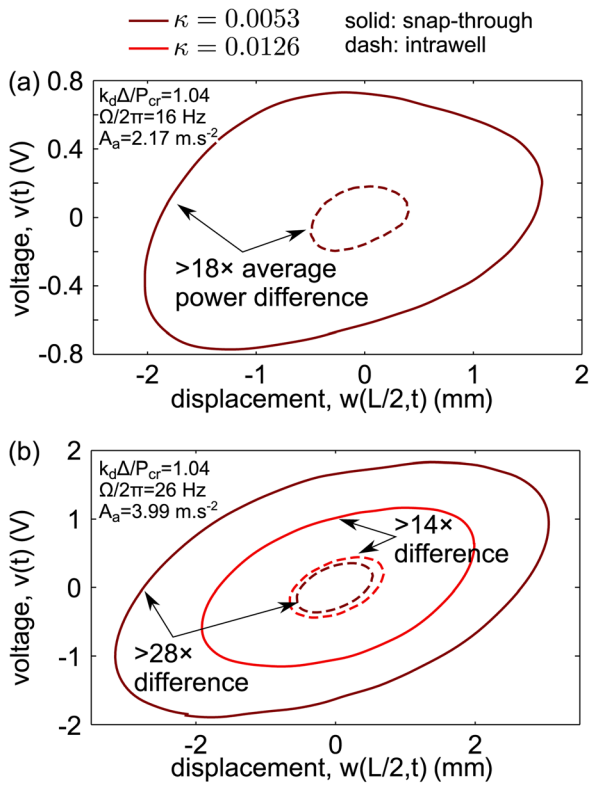

Fig. 7 Experimentally measured phase plane trajectories of voltage and beam center bending displacement for preload ratio of 1.04 for the harvester platform configurations exhibiting coexisting dynamic regimes. (*a*) Base acceleration amplitude of 2.17 m s^{-2} and frequency of 16 Hz. (*b*) Base acceleration amplitude of 3.99 m s^{-2} and frequency of 26 Hz. Average power differences are quoted for the various pairs of coexisting dynamics.

devices for their improved energy harvesting potential dictates that the structures be operated under excitation conditions which do not promote the coexisting regimes.

Figures 8(*a*) and 8(*b*) show measured and predicted voltage amplitudes, respectively, when the platforms are excited at a frequency of 26 Hz across a varying range of base acceleration amplitudes. Among the findings, the increased likelihood for coexisting dynamics is seen in Fig. 8, even for the platform having an axial stiffness ratio of 0.0426 which is marginally monostable. For the bistable architectures, $\kappa = 0.0126$ and 0.0053, the potential for coexisting intrawell and snap-through dynamics is more likely across a large range of base acceleration amplitudes than was the case found at the excitation frequency of 16 Hz in Fig. 6. Despite such a trend, computations taken from the phase trajectories in Fig. 7(*b*) indicate that with base acceleration amplitude at 3.99 m s^{-2} and frequency 26 Hz, the advantage of achieving the snap-through dynamic for the softest case of axial suspension, $\kappa = 0.0053$, is more than a 28 times enhancement in average power. Clearly, a tradeoff exists between obtaining greater average powers using softer axial suspensions and an increased potential for activating the undesired intrawell oscillations. Effective utilization of the axial suspension and compression features therefore must carefully consider the excitation environment with respect to the device design.

5 Origin of Performance Enhancement by Softer, Axially Compressed Suspensions

The theme of the discoveries in Secs. 2 and 4 is that the compression of the simply supported energy harvesting beams and the utilization of more compliant axial suspension stiffness leads to dramatic improvement of the average power generation, particularly at lower frequencies of harmonic excitation. Yet, the findings themselves do not explain the *origin* of such enhancements. To look more deeply into the source of the performance benefits, Fig. 9 plots the percentage contributions of the three primary potential energy resources using results which are obtained by the analytical model for a base acceleration amplitude of 1.50 m s^{-2}, frequency of 18.25 Hz, and axial compressive preload ratio of 1.04. Recall that under such compressive forces, the device design with the least compliant axial suspension stiffness ($\kappa = 0.300$) remains monostable whereas the device using the most compliant axial stiffness ($\kappa = 0.0053$) is statically bistable. For these two device designs, Fig. 9 shows that the conventional simply supported energy harvester (having the least compliant axial stiffness) exhibits a nearly equivalent distribution of potential energy manifest as stretching the beam axially as in bending the beam. Yet, it is bending of the energy harvesting beam that has far more influence toward the overall transduced voltage by the applied PVDF piezoelectric layers. Considering the data for the most compliant axial suspension stiffness ($\kappa = 0.0053$), Fig. 9 indicates that the beam bending potential energy is considerably increased while the axial stretching of the beam is almost eliminated. In other words, the greater suspension compliance promotes beam bending at the expense of beam axial stretching, which thereafter has the effect of more readily activating snap-through. The origin of the performance enhancement is therefore the redistribution of potential energy among the primary contributors, achieved using the strategic selection of the axial compressive force and the axial suspension spring stiffness, which are characterized using the preload ratio and axial stiffness ratio, respectively.

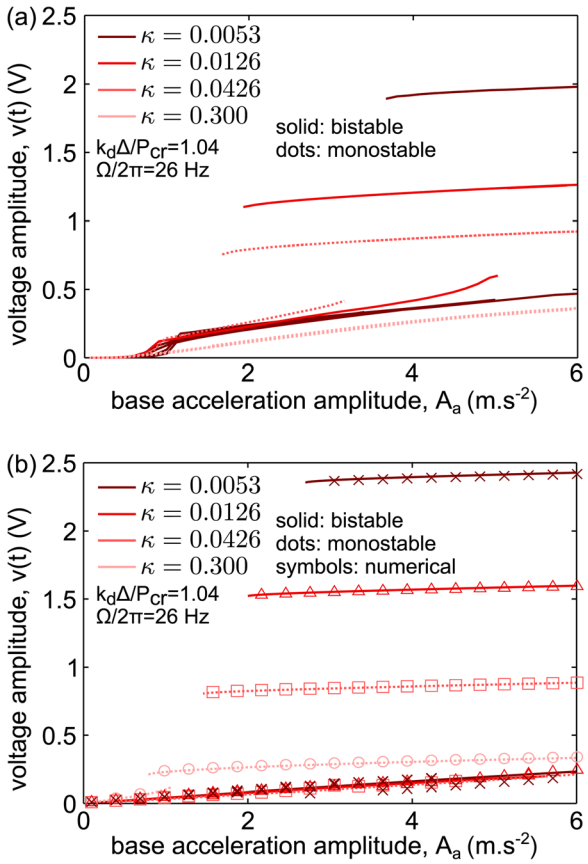

Fig. 8 Voltage across load resistance for preload ratio of 1.04 and excitation frequency of 26 Hz: (*a*) experimental measurements and (*b*) analytical and numerical results

6 Conclusions

This research shows that leveraging additional axial compliance and nonlinearities can lead to significant improvement in the effectiveness of vibration energy harvesting beam systems and that uncovering the origin of the enhancements may guide designs best suited to the available vibration resources. A simply supported energy harvesting beam, axially compressed on one end and suspended by an axial spring on the other, is developed according to a biologically inspired structural concept. When compared to the conventional design that employs axially fixed simple supports, the new harvester architecture is found to enable a substantial increase in average power generation across a wide range of excitation frequencies and amplitudes. The soft, compliant axial supports favorably distribute the dynamic storage and release of potential energy among the various primary contributors, thus maximizing the bending of the beam which is the principal source of the net electromechanical transduction. By these insights, the utilization of compressed axial suspensions may more readily enhance the performance of energy harvesting beam systems under the challenging excitation spectra typical of environmental vibrations.

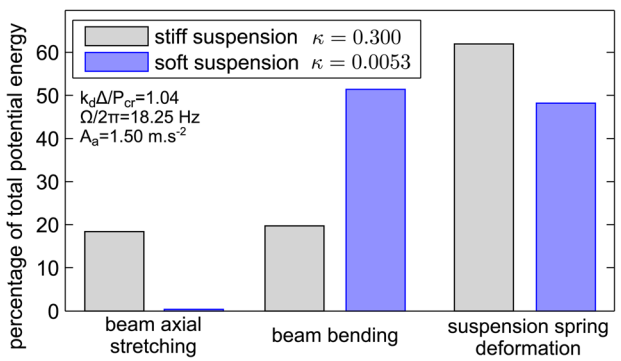

Fig. 9 Percentage distribution of potential energy per excitation cycle among the three primary contributors: axial stretching of the beam, beam bending, and deformation of the suspension spring. Results shown for the energy harvesters employing the most stiff suspension (conventional design) and the softest suspension stiffness. Preload ratio 1.04. Base acceleration amplitude 1.50 m s^{-2} and frequency 18.25 Hz.

Acknowledgment

This research was supported by the National Science Foundation under Award No. 1232436 and by the University of Michigan Collegiate Professorship.

Appendix

In the following, the subscript notations b and p continue to denote the beam and piezoelectric layers, respectively. Additionally, the moments of inertia are $I_{b,p} = h_{b,p}t_{b,p}^3/12$.

$$M^* = \frac{1}{2}\rho_b A_b L_b + 2\rho_p A_p \int_{l_1}^{l_2} \phi^2 \mathrm{d}x + m_a r_a^2 \left(\frac{\pi}{L_b}\right)^2 \tag{A1}$$

$$C^* = \frac{1}{2} c_b L_b \tag{A2}$$

$$K^* = \frac{1}{2} E_b I_b L_b \left(\frac{\pi}{L_b}\right)^4 + 2E_p I_p \int_{l_1}^{l_2} \phi_{xx}^2 \mathrm{d}x \tag{A3}$$

$$K_p^* = \frac{1}{2} L_b \left(\frac{\pi}{L_b}\right)^2 \tag{A4}$$

$$F_1^* = \frac{1}{4} E_b I_b L_b \left(\frac{\pi}{L_b}\right)^6 + 4E_p I_p \int_{l_1}^{l_2} \phi_{xx}^2 \phi_x^2 \mathrm{d}x \tag{A5}$$

$$F_2^* = \frac{1}{8} E_b A_b L_b \left(\frac{\pi}{L_b}\right)^4 \tag{A6}$$

$$H^* = G\left[\frac{2}{\pi}\rho_b A_b L_b + 2\rho_p A_p \int_{l_1}^{l_2} \phi \mathrm{d}x\right] \tag{A7}$$

where it is assumed that the body forces $s(x)$ result from gravitational influences having acceleration of G

$$Z^* = \frac{2}{\pi}\rho_b A_b L_b + 2\rho_p A_p \int_{l_1}^{l_2} \phi \mathrm{d}x \tag{A8}$$

$$C_p^* = 2\left(\frac{A_p}{t_p^2}\right)\varepsilon_{33}(l_2 - l_1) \tag{A9}$$

$$\theta^* = 2\left(\frac{A_p \bar{t}_p}{t_p}\right) e_{31} \int_{l_1}^{l_2} \phi_{xx} \mathrm{d}x \tag{A10}$$

$$\theta_{NL}^* = 2\left(\frac{A_p \bar{t}_p}{t_p}\right) e_{31} \int_{l_1}^{l_2} \frac{1}{2} \phi_{xx} \phi_x^2 \mathrm{d}x \tag{A11}$$

References

[1] Elvin, N., and Erturk, A., 2013, *Advances in Energy Harvesting Methods*, Springer, New York.

[2] Daqaq, M. F., Masana, R., Erturk, A., and Quinn, D. D., 2014, "On the Role of Nonlinearities in Vibratory Energy Harvesting: A Critical Review and Discussion," ASME Appl. Mech. Rev., **66**(4), p. 040801.
[3] Aladwani, A., Arafa, M., Aldraihem, O., and Baz, A., 2012, "Cantilevered Piezoelectric Energy Harvester With a Dynamic Magnifier," ASME J. Vib. Acoust., **134**(3), p. 031004.
[4] Yang, J., Wen, Y., and Li, P., 2011, "Magnetoelectric Energy Harvesting From Vibrations of Multiple Frequencies," J. Intell. Mater. Syst. Struct., **22**(14), pp. 1631–1639.
[5] Gu, L., and Livermore, C., 2011, "Impact-Driven, Frequency Up-Converting Coupled Vibration Energy Harvesting Device for Low Frequency Operation," Smart Mater. Struct., **20**(4), p. 045004.
[6] Galchev, T., Kim, H., and Najafi, K., 2011, "Micro Power Generator for Harvesting Low-Frequency and Nonperiodic Vibrations," J. Microelectromech. Syst., **20**(4), pp. 852–866.
[7] Halvorsen, E., 2013, "Fundamental Issues in Nonlinear Wideband-Vibration Energy Harvesting," Phys. Rev. E, **87**, p. 042129.
[8] Green, P. L., Worden, K., Atallah, K., and Sims, N. D., 2012, "The Benefits of Duffing-Type Nonlinearities and Electrical Optimisation of a Mono-Stable Energy Harvester Under White Gaussian Excitations," J. Sound Vib., **331**(20), pp. 4504–4517.
[9] Leadenham, S., and Erturk, A., 2014, "M-Shaped Asymmetric Nonlinear Oscillator for Broadband Vibration Energy Harvesting: Harmonic Balance Analysis and Experimental Validation," J. Sound Vib., **333**(23), pp. 6209–6223.
[10] Meimukhin, D., Cohen, N., and Bucher, I., 2013, "On the Advantage of a Bistable Energy Harvesting Oscillator Under Bandlimited Stochastic Excitation," J. Intell. Mater. Syst. Struct., **24**(14), pp. 1736–1746.
[11] Zhao, S., and Erturk, A., 2013, "On the Stochastic Excitation of Monostable and Bistable Electroelastic Power Generators: Relative Advantages and Tradeoffs in a Physical System," Appl. Phys. Lett., **102**(10), p. 103902.
[12] Cao, J., Zhou, S., Inman, D. J., and Lin, J., 2015, "Nonlinear Dynamic Characteristics of Variable Inclination Magnetically Coupled Piezoelectric Energy Harvesters," ASME J. Vib. Acoust., **137**(2), p. 021015.
[13] Harne, R. L., and Wang, K. W., 2013, "A Review of the Recent Research on Vibration Energy Harvesting Via Bistable Systems," Smart Mater. Struct., **22**(2), p. 023001.
[14] Tang, L., and Yang, Y., 2012, "A Nonlinear Piezoelectric Energy Harvester With Magnetic Oscillator," Appl. Phys. Lett., **101**(9), p. 094102.
[15] Wu, Z., Harne, R. L., and Wang, K. W., 2014, "Energy Harvester Synthesis Via Coupled Linear-Bistable System With Multistable Dynamics," ASME J. Appl. Mech., **81**(6), p. 061005.
[16] Chen, L. Q., and Jiang, W. A., 2015, "Internal Resonance Energy Harvesting," ASME J. Appl. Mech., **82**(3), p. 031004.
[17] Thomson, A. J., and Thompson, W. A., 1977, "Dynamics of a Bistable System: The Click Mechanism in Dipteran Flight," Acta Biotheor., **26**(1), pp. 19–29.
[18] Miyan, J. A., and Ewing, A. W., 1985, "How Diptera Move Their Wings: A Re-Examination of the Wing Base Articulation and Muscle Systems Concerned With Flight," Philos. Trans. R. Soc. London, Part B, **311**(1150), pp. 271–302.
[19] Timoshenko, S. P., 1936, *Theory of Elastic Stability*, McGraw-Hill, New York.
[20] http://upload.wikimedia.org/wikipedia/commons/8/8f/Housefly_anatomy-key.svg
[21] Harne, R. L., and Wang, K. W., 2015, "Dipteran Wing Motor-Inspired Flapping Flight Versatility and Effectiveness Enhancement," J. R. Soc. Interface, **12**(104), p. 20141367.
[22] Dickinson, M. H., and Tu, M. S., 1997, "The Function of Dipteran Flight Muscle," Comp. Biochem. Physiol., Part A, **116**(3), pp. 223–238.
[23] Rao, S. S., 2004, *Mechanical Vibrations*, 4th ed., Pearson Prentice Hall, Upper Saddle River, NJ.
[24] Meirovitch, L., 1967, *Analytical Methods in Vibration*, Macmillan, New York.
[25] Hodges, D. H., 1984, "Proper Definition of Curvature in Nonlinear Beam Kinematics," AIAA J., **22**(12), pp. 1825–1827.
[26] Preumont, A., 2006, *Mechatronics: Dynamics of Electromechanical and Piezoelectric Systems*, Springer, Dordrecht.
[27] Mayers, J., and Wrenn, B. G., 1964, "Combined Influence of Higher-Order Linear Effects and Nonlinear Effects on the Lateral Vibration Behavior of Solid and Sandwich Beams," Department of Aeronautics and Astronautics, Stanford University, Stanford, CA, SADAER Report No. 208.
[28] Wagg, D., and Neild, S., 2010, *Nonlinear Vibration With Control: For Flexible and Adaptive Structures*, Springer, Dordrecht.
[29] Inman, D. J., 2001, *Engineering Vibration*, Prentice Hall, Upper Saddle River, NJ.
[30] Wu, Z., Harne, R. L., and Wang, K. W., 2015, "Excitation-Induced Stability in a Bistable Duffing Oscillator: Analysis and Experiment," ASME J. Comput. Nonlinear Dyn., **10**(1), p. 011016.
[31] Geiyer, D., and Kauffman, J. L., 2015, "Chaotification as a Means of Broadband Energy Harvesting With Piezoelectric Materials," ASME J. Vib. Acoust., **137**(5), p. 051005.